On the use of α-shapes for the measurement of 3D bubbles in fluidized beds from Two-Fluid Model simulations

Ignacio Julián[1], David González[2], Javier Herguido[1], Miguel Menéndez[1]

[1]*Catalysis, Molecular Separations and Reactor Engineering Group (CREG), Department of Chemical and Environmental Engineering*
[2]*Applied Mechanics and Bioengineering group (AMB), Department of Mechanical Engineering*

Aragon Institute of Engineering Research (I3A), Universidad de Zaragoza, 50018 Zaragoza, Spain

Abstract

A geometrical technique based on shape construction was employed to reconstruct the simulated domain of 3D bubbles in a gas-solid fluidized bed, from Two-Fluid Model (TFM) simulations. The Delaunay triangulation of the cloud of points that represent volume fraction iso-surfaces in transient TFM simulations was filtered by means of the so-called α-shapes, allowing a topologically accurate description of 3D bubbles within a fluidized bed. Consequently, individual 3D bubble properties such as size and velocity were measured. Simulated bubble characteristics were further compared to those measured on pseudo-2D bed facilities by image techniques in order to illustrate the effect of the bed geometry on the bubbling behaviour under mimicked operational conditions.

Keywords

Fluidized bed, bubble hydrodynamics, 3D bubble measurement, Delaunay triangulation, alpha-shape

1. Introduction

Fluidized beds provide an efficient mass and heat transfer due to their characteristic high fluid-solid contact area, high relative velocity between phases and high level of particulate mixing. For this reason, fluidization technology is widely used in industry for a number of physical and chemical processes involving catalytic reactions, mixing or drying [1]. Since the fluid dynamic performance of a fluidized bed determines its efficiency, it is essential to understand the behaviour of the multiphase flow in such a system. In particular, it is very important to analyze the bubbling regime within a fluidized bed, since bubbles promote solids axial mixing and determine mass and heat transfer limitations [1].

The complete understanding of the fluidization dynamics is very challenging. Many efforts have done in the last five decades in this field, both experimentally and with the aid of computational models. Reported experimental works are mainly focused on the fluid dynamic analysis of pseudo-2D beds by optical techniques (basically Particle Image Velocimetry (PIV) and Digital Image Analysis (DIA)), which are normally preferred due to their non-intrusiveness, ease of implementation and large amount of available data from visual access [2-4]. The main

drawback of these techniques is the need of visual access. Since dense gas-solid flows are typically opaque to visible light, this limits the use of the technique to 2D systems although most of the fluidized beds are cylindrically shaped [5]. To circumvent this limitation, some techniques were developed to characterize experimental 3D beds by means of non-intrusive tomography (electric capacitance tomography [6] or nuclear tomography [7]), particle tracking techniques [8-10], optical and capacitance probes [11, 12] or pressure transducers [13]. Excluding particle tracking techniques, which are developed to follow the motion of single particles, the above mentioned techniques allow the detection of local voidage in the bed, i.e. the measurement of the gas-solids distribution in 3D fluidized beds. In any case, the reconstruction of the experimentally measured signals into 3D bed porosity maps or bubbling characterization is quite troublesome [14].

On the other hand, simulation studies on bubbling characterization do not deal with the visual access, intrusiveness or data reconstruction issues but with the computational cost of the available literature models. Modeling of 3D fluidized beds can be used to provide instantaneous, whole-field information on the bubble behavior in geometries close to real ones, improving scale up advantages [15]. As a multiphase flow, the fluidized bed dynamics can be simulated basically according to three different models regarding the required degree of detail: direct numerical simulation, discrete particle model and continuum model based on the kinetic theory of granular flow [16]. Direct numerical simulation techniques, including Lattice-Boltzmann or Front-Tracking methods, reveal detailed gas-particles interactions [17] but they are nowadays limited to the study of very small beds with low number of particles due to their high computational cost. Discrete particle models, i.e. Eulerian-Lagrangian approach, provide relevant information about the particle-particle collisions and the solids mixing within the bed [18]. However, in spite of the increasing computational capacity over the last decade, they are still limited to the simulation of lab scale and medium-size fluidized beds. The continuum model, Eulerian-Eulerian or Two-Fluid Model depicts both gas and dense phase in the fluidized bed as interpenetrating continua, thus, reducing the computational cost and allowing the simulation of large scale structures for either pseudo-2D and 3D bed configurations [16].

The analysis of bubble hydrodynamics from transient Two-Fluid Model (TFM) results performed in 2D or pseudo-2D beds is well described by many authors in literature [19-23]. Basically, a prescribed threshold void fraction (normally in the range 0.70 – 0.85, according to several authors [19-21, 24-26]) is used to discriminate gas bubbles from the dense phase in the transient bed porosity maps. Image Processing algorithms binarize the obtained voidage maps to identify bubble contours and calculate bubble properties such: equivalent diameter, aspect ratio or bubble centroid location. By measuring the displacement of a single bubble centroid between subsequent frames, the bubble velocity is obtained.

However, the analysis of bubble characteristics from TFM simulations of 3D fluidized beds is not straightforward. Although commercial Computational Fluid Dynamic (CFD) codes are able to post-process transient results to show bubble contours by means of void fraction iso-surfaces, these software are not able to discriminate single gas bubbles. Therefore, bubble data such as size, aspect ratio or spatial location of the bubble centroid cannot be directly

extracted from simulation results. Some authors [15] use tomography techniques to get radial voidage maps at different bed heights and then carry out image reconstruction to estimate 3D bubble characteristics. Some others [27] couple porosity maps and bubble shape factors from single detached bubble simulations [28] to estimate the 3D bubble characteristics.

On the one hand, the latter technique requires some assumptions regarding bubble sphericity that may affect the accuracy of the results. On the other hand, the tomography reconstruction implies the concatenation of a series of two dimensional sliced images through the bed vertical axis to form transient 3D spatial images from which bubbles are identified. The 3D bubble volume estimation from 2D planar porosity maps is computationally expensive and the accuracy of the method depends on the number of sliced planes considered in the 3D image reconstruction [15].

Therefore, taking advantage of the characteristic fixed mesh which is used in the Two-Fluid Model formulation for the simulation of the fluidized bed dynamics, this work suggest a direct method to quantify 3D bubble properties from nodal results applying a geometric construction technique, the so-called α*-shape method* introduced by Edelsbrunner and Mücke (1994) [29]. The use of α-shapes allows a topological reconstruction of individual bubbles creating unconnected subdomains whose contours are the individual bubble boundaries. The accuracy of the bubble contour reconstruction depends on the computational mesh size, i.e. the distance between adjacent mesh nodes. The geometric reconstruction based on α-shapes, which is extensively applied in other fields such medical image analysis or molecular structure modeling, is here used for the first time (to the best knowledge of the authors) to identify and measure gas bubbles in simulated 3D fluidized beds.

This study specifically focuses on the detection and measurement of 3D bubbles in a particular fluidized bed reactor configuration: the Two-Section Two-Zone Fluidized Bed Reactor (TS-TZFBR) showed in Figure 1.a. This reactor has been described elsewhere [30] as a potential tool for process intensification in the field of heterogeneous catalysis due to its ability to perform heterogeneous catalytic reactions and catalyst regeneration in a single vessel. Two separated gas inlets along the bed, through which the reactive and regenerative gas flows are fed, induce two bed zones with different atmospheres. The bed fluidization, i.e. the catalyst circulation, between the two zones allows the process integration [30]. The performance of this kind of reactor arrangement has been successfully tested in many processes such as: light alkane dehydrogenations, ethanol steam reforming or methane aromatization [31-33]. Its fluid dynamic characteristics have also been extensively studied both experimentally and with TFM simulations on pseudo-2D reactor geometries [24, 34-37]. In these studies, some relevant results regarding the most suitable reactor geometry to avoid defluidization phenomena were presented. Besides, in order to favor solids axial mixing and minimize mass transfer limitations an operational window for the inlet gas flow was defined. Nevertheless, all these studies were performed on pseudo-2D TS-TZFBR configurations.

Therefore, with the present work authors aim to study the potentials of the α-shapes method to identify and measure volumetric gas bubbles in simulated three-dimensional fluidized beds. As a first approach, a formulation of the TFM that was previously validated with experimental

data for pseudo-2D TS-TZFBR [23] has been used to perform the 3D fluid dynamic simulations. The model closures and parameter values were adapted to the pseudo-2D system and might not give physical realistic predictions of a 3D TS-TZFBR bed, as already observed by some authors [38, 39]. The qualitative comparison of the model predictions on the bubbling characteristics performed in this work for both bed configurations aims to bring some light on the extrapolation of pseudo-2D bubble data to the real 3D column bubbling.

2. Simulations

Eulerian three-dimensional simulations were performed using commercial Ansys CFX 14.5 software. The Eulerian model that considers both solid and gas phase as interpenetrating continua introduces the concept of phase volume fraction [40]. The model equations consider mass and momentum conservation for each phase, *i* (gas or solid), Ec. 1 – 3.

$$\frac{\partial}{\partial t}(\varepsilon_i \rho_i) + \nabla \cdot (\varepsilon_i \rho_i \, \vec{v}_i) = 0 \tag{1}$$

$$\frac{\partial}{\partial t}\left(\varepsilon_g \rho_g \, \vec{v}_g\right) + \nabla \cdot \left(\varepsilon_g \rho_g \, \vec{v}_g \vec{v}_g\right) = -\varepsilon_g \nabla P + \varepsilon_g \nabla \cdot \bar{\bar{\tau}}_g + \varepsilon_g \rho_g \bar{g} + K_{gs}(\vec{v}_g - \vec{v}_s) \tag{2}$$

$$\frac{\partial}{\partial t}(\varepsilon_s \rho_s \, \vec{v}_s) + \nabla \cdot (\varepsilon_s \rho_s \, \vec{v}_s \vec{v}_s) = -\varepsilon_s \nabla P - \nabla P_s + \varepsilon_s \nabla \cdot \bar{\bar{\tau}}_s + \varepsilon_s \rho_s \bar{g} + K_{gs}(\vec{v}_s - \vec{v}_g) \tag{3}$$

The left hand side of the momentum conservation equation represents the temporal and spatial transport terms. The right hand side represents the various interacting forces: buoyancy, pressure drop, viscous stress, gravity and interphase drag force. K_{gs} is the interphase momentum exchange coefficient whereas $\bar{\bar{\tau}}_i$ is the *i* phase stress-strain tensor.

The solution of this set of partial differential equations requires some closures to describe the interaction between phases. In this study the computational model described by Julián et al. [24] in a previous work on pseudo-2D TS-TZFBR was used to simulate the fluid dynamic behaviour of the 3D reactor configuration using the element-based finite volume method of Ansys CFX. Concretely, the solid-fluid interphase momentum exchange coefficient was modeled with the Gidaspow drag function [40], that combines the equations of Wen and Yu and Ergun for the interphase drag force, where C_D was estimated using the Schiller-Naumann drag coefficient model [41]. The interphase stress-strain tensor for the phase *i* (either gas or solid) was assumed to follow the Newtonian strain-rate relation, which depends on the bulk and shear viscosities. The shear viscosity was estimated as the sum of the collisional, frictional and kinematic contributions. Both the bulk and shear viscosities depend on the granular temperature and a collisional restitution coefficient [42]. In this study, the restitution coefficient was set to 0.95 for all simulations following the recommendations of Julián et al. [24]. The angle of internal friction, φ, was set to 30º and the radial distribution function, g_0, (which measures the average distance between particles) was modeled according to the description of Lun and Savage [43]. The granular temperature was determined algebraically under the assumption of local equilibrium in a transport equation model, i.e. energy production equals energy dissipation. This assumption is often used in dense, slow moving fluidized beds where the local generation and dissipation of granular temperature far outweigh the transport by convection and diffusion [44]. Lastly, the solids pressure was

modeled according to the kinetic theory model of gases [42], being adapted to consider the inelastic collisions between particles. The maximum solid packing, $\varepsilon_{s,m}$, was set to 0.65. A monodisperse 200 μm particle size distribution, which agrees with the particle size used in previous experimental works, was used in the simulations throughout the study. The set of governing equations is detailed in Table 1.

2.1 Computational domain

The computational domain is presented in Figure 1.b. The three dimensional reactor is 50 cm high, having an external diameter of 8 cm in the upper region and 4 cm in the lower bed zone. The two cylindrical regions are connected by a tronco-conical section with an inclination of 80^o with respect to the horizontal axis. The narrower cylindrical section (i.e. 'regeneration zone') is 12 cm high. Additionally, the characteristic gas inlet through an intermediate bed height in a TS-TZFBR is simulated erecting a vertical tube wall (3 mm external diameter) having four cross-orifices for gas inlet in its bottom end. The length of each distributor blade is 1 cm and the diameter of the orifices is 3 mm. The internal gas inlet is located 12 cm above the bottom of the bed, thus, at the same height as the top end of the narrower bed cross-section. Both the tapered angle and the axial location of the immersed gas distributor have been described elsewhere [24, 36, 37] to be suitable to avoid defluidization effects and short-circuiting in the solids recirculation.

Mesh independence studies were conducted to find suitable conditions in terms of computational cost, numerical stability and reproducibility of hydrodynamic results. The domain was finally discretized by more than 10^5 nodes, with adaptive mesh size between 1 and 2.5 mm (Figure 1.c). CFD simulations were solved using a time step, $\Delta t = 10^{-4}$ s.

2.2 Boundary conditions and solver settings

The bulk mass flow rate was selected as the boundary condition for the reactor gas inlets to avoid dense phase outflow. An opening boundary was applied to the reactor outlet at the top of the domain. The opening condition refers to the unrestricted circulation of gas and dense phase (if it eventually reaches the top of the bed) through the boundary. The flow direction through inlets and outlets was defined as normal to the boundary surface and the relative pressure on the domain outlets was set to 0 Pa, i.e. $P = P_{atm}$. A no-slip condition was applied for the gas phase at the walls. Regarding the particle-wall interaction, the proper selection of the wall boundary condition for the solids phase is not straightforward for Euler-Euler models and different formulations can be found in the open literature: no-slip, partial-slip and free-slip, e.g. [44, 45] conditions. Although it seems that the partial-slip is the most realistic approach, the selection of a proper specularity coefficient is not trivial and needs to be done carefully. Since the detailed analysis of the wall-particle friction is out of the scope of this work, a no-slip boundary condition was applied for the gas dense phase as a first approach. The set of partial differential equations was solved using a SIMPLE scheme (Semi Implicit Method for Pressure Linked Equations) for pressure correction. In this algorithm, the velocity field is first predicted based on the pressure field from the previous iteration and then

iteratively corrected using the mass and momentum equations to maintain incompressibility of both phases [26]. A first order Backward Euler method was used for the discretization of the transient terms. The second order time discretization is usually preferred for accurate solution of fast-moving riser flows with the TFM but this is not the case for dense bubbling beds at low relative gas velocities, in which the majority of the bed moves relatively slowly [38, 46]. The numerical discretization of the system variables was done with an upwind scheme with convergence criteria based on a RMS residual target of 10^{-3}, as recommended from previous works [24]. CFD simulation parameters are listed in Table 2.

To obtain fully comparable results in terms of bed height fluctuation between pseudo-2D and 3D simulations, the total volume of the domain was initially filled with a 25% of solids, which settle in the absence of fluidization gas (sedimentation stage), following a previously described method [24].

3. Bubble discrimination

Transient TFM simulation results contain information about system variables, e.g. phase volume fraction, at every mesh node within the simulation domain. As an example, Figure 2.a illustrates the transient solids volume fraction map at a central xz plane of a 3D TFM simulation on a TS-TZFBR reactor configuration. The iso-surfaces tool, which is a common data visualization method available in the majority of CFD post-processing software, allows the visualization of regions with a constant property value within the computational domain. In order to identify bubble boundaries, a prescribed solids volume fraction $\varepsilon_s = 0.15$ was defined as a threshold value for the iso-surfaces method following the recommendations of some authors [19-21, 39]. Figures 2.b and 2.c. illustrate the bed regions detected as bubble contours after applying iso-surfaces threshold porosity. The domain defined by the iso-surfaces enclosed, then, a list of spatial coordinates of the mesh nodes (Figure 2.d) that accomplish the given restriction: $\varepsilon_s = 0.15$.

Once the list of bubble-boundary nodes was determined, a Delaunay triangulation algorithm was applied (using the Computational Geometry toolbox of Matlab R2010b) to connect every node by means of unique tetrahedral shapes. The algorithm itself did not discriminate nodes that belong to different bubbles. For this reason it was necessary to constrain node connections in order to identify 'false' connections and remove them, generating multiple domains: one for each bubble (Figure 2.e).

The filtration of the Delaunay triangulation was carried out using the α-shapes geometric method. To the best knowledge of the authors, this is the first time that this method was applied for bubble volume reconstruction in 3D fluidized bed simulations. Therefore, the description and validation of the method for the characterization of 3D bubbles in simulated gas-solid fluidized beds represents the main contribution of this work.

The α-shapes were firstly proposed by Edelsbrunner and Mücke [29] and deal with the elimination of all tetrahedra whose circumscribing radius, i.e. mesh size in finite element terminology, is greater than a prescribed level of detail for the geometry, α. Main drawbacks of the technique are the selection of a suitable α value and the fact that α-shapes only work well for a uniform concentration of points [47]. This is the case of the Eulerian approach, in which

the nodes of the computational mesh remain fixed in the space along the time. Since the distance between nodes in the fixed adaptive mesh used in this work ranges from 1 to 2.5 mm, the minimum α value that allows the discrimination of adjacent bubbles is the maximum distance between connected nodes in the mesh. In other words, all connections (from the Delaunay triangulation) made between nodes that are separated by a spatial distance greater than α = 2.5 mm are removed by the α-shape method. Analogously for a 3D grid, the volume of a regular tetrahedron with 2.5 mm long edges represents the threshold volume over which tetrahedra are removed from the Delaunay triangulation domain.

Otherwise, adjacent bubbles separated by less than 2.5 mm are computed as a single bubble. Although this may cause discrepancies in the analysis of bubble characteristics in bubble columns, where bubble clusters or swarms are formed under certain gas flow regimes, this should not represent an important issue in gas-solid fluidized beds at bubbling or slugging regimes. At these regimes, gas bubbles appear fairly isolated from each other and only coalescence and break up phenomena could compromise the accurate discretization of bubbles by the suggested α-shape method.

Once false node connections are removed, the volume and centroid (center of mass) of each isolated bubble domain can be calculated using equations 4 and 5. In equation 4, $v_{b,i}$ is the volume of the transient bubble *i* which is calculated as the sum of volumes of the "*T*" tetrahedra that form the bubble domain. *A*, *B*, *C* and *D* are the nodes of the tetrahedron "*t*" with spatial coordinates (*x*, *y*, *z*) as illustrated in Figure 3. In equation 5, $b_{CoM,i}$ is the center of mass of the bubble *i*, *N* is the number of nodes that form bubble *i* being $(n_x, n_y, n_z)_n$ the spatial coordinates of the node *n*.

$$v_{b,i} = \sum_{t=1}^{T} \left(\frac{1}{6} \begin{vmatrix} A_x & B_x & C_x \\ A_y & B_y & C_y \\ A_z & B_z & C_z \end{vmatrix} \right)_t = \sum_{t=1}^{T} \left(\frac{1}{6} \overline{AD} \cdot (\overline{BD} \times \overline{CD}) \right)_t \tag{4}$$

$$b_{CoM,i}(x,y,z) = \frac{1}{N} \left(\sum_{n=1}^{N} (n_x)_n \, , \sum_{n=1}^{N} (n_y)_n \, , \sum_{n=1}^{N} (n_z)_n \right) \tag{5}$$

The 3D equivalent bubble diameter (d_b) is determined as the diameter of the sphere that occupies the same volume as the bubble (equation 6), whereas the average equivalent bubble diameter at certain bed vertical position is calculated according to the equation 7. This expression, which has already been used in previous studies [24, 31, 35], weights bubble diameters proportionally to their size. The use of the weighted average d_b is motivated by the fact that big bubbles are more representative of the bubbling gas flow than small spurious bubbles. Moreover, from a fluid dynamic point of view, the larger bubbles have a greater influence on the mixing of solids in the fluidized bed than smaller ones.

$$d_{b(3D),i} = 2 \left(\frac{3}{4\pi} v_{b,i} \right)^{1/3} \tag{6}$$

$$\overline{d_b}(z) = \frac{\sum_{n=1}^{N} {d_{b,i}}^2(z)}{\sum_{n=1}^{N} d_{b,i}(z)} \tag{7}$$

The bubble velocity is calculated comparing bubble centroid locations between subsequent transient fluidization frames. A nearest-neighbour algorithm [48] is used to identify bubbles and track their displacement between shortly delayed simulation time steps, $\Delta t = 10^{-2}$ s. Bubble data concerning volume, aspect ratio and centroid coordinates (*x, y, z*) are compared between consecutive transient results. The bubble identification is carried out by minimization of the global 'distance' between bubble data at the analyzed time steps under certain restrictions:

a) The axial coordinate of the bubble centroid at the previous time step cannot be greater than that at the later one, i.e. negative bubble velocities are not computed;

b) The equivalent diameter of an individual bubble cannot change in more than 20% between consecutive frames [49];

c) Each bubble data at the latter time step can have as maximum one correspondence to a bubble data at the previous time step. The determination of bubble velocity in case of bubble break-up or coalescence is, thus, avoided to prevent average u_b results to be influenced by wrong bubble tracking.

The statistical bubble size and velocity distribution in pseudo-2D and 3D fluidized beds is strongly dependant on the way to compute bubble data. In this work, several methods have been implemented to carry out a consistent comparison between bubbling results obtained for the two different reactor configurations. Concretely, two different approaches have been considered to compute the equivalent bubble diameter in pseudo-2D and 3D beds: the volumetric and the superficial formulation. As a result, four equivalent bubble diameters are considered:

1) 3D bed + volumetric formulation: equivalent diameter of the sphere that encloses the same volume as the bubble (equation 6).

2) 3D bed + superficial formulation: equivalent diameter of the circle that encloses the same area as that projected by the bubble through the plane that crosses the bed center axially (equation 8).

3) pseudo-2D + volumetric formulation: equivalent diameter of the cylinder that encloses the same volume as the bubble (equation 9).

4) pseudo-2D + superficial formulation: equivalent diameter of the circle that encloses the same area as that projected in the front face of the bed (equation 8).

The suggested α-shapes method (Figure 2.e) applies only for the first case, i.e. the determination of the equivalent bubble diameter in 3D beds based on the gas volume enclosed by bubbles.

In the remaining cases, the equivalent bubble size can be determined using Digital Image Analysis (DIA) techniques. Such techniques discriminate gas bubbles from the emulsion phase by means of pixel intensity in the solids volume fraction distribution maps and have been widely reported in literature [2-6]. Applied to 3D simulations, the DIA algorithm detected bubble contours in 2D void fraction maps traced through the 3D bed center (Figure 4.a). Similarly, the DIA processing of the facial transient porosity distribution was employed to

determine planar bubble characteristics in the pseudo-2D bed. In both cases, the bubble size was determined from the equivalent diameter of a circle which surface had the same area as the projected bubble in the plane (Equation 8), as shown in Figure 4.b.

Additionally, a formulation that takes into account the volume enclosed in pseudo-2D bubbles (Equation 9) was used to describe the equivalent bubble diameter as the diameter of a sphere that occupied the same volume as the projected bubble area (A_b) through the bed depth (L_{bed}), as shown in Figure 4.c.

$$d_{b(area),i} = 2\left(\frac{A_{b,i}}{\pi}\right)^{1/2} \tag{8}$$

$$d_{b(volume),i} = 2\left(\frac{3}{4\pi}A_{b,i}L_{bed}\right)^{1/3} \tag{9}$$

Concerning the statistical analysis of the bubble size profile along the vertical bed position, $d_b(z)$, the time-averaged axial distribution of the equivalent bubble diameter was obtained either by computing raw bubble data or just by using those bubbles that were identified at consecutive frames, i.e. bubbles whose rising velocity was determined from subsequent porosity maps. Therefore, spurious bubbles were filtered out from the bubble data statistics.

4. Results

In this section, the most relevant results regarding the use of α-shapes in bubble discrimination are presented. Besides, a critical comparison between the TFM simulation results of bubbling regimes obtained for 2D and 3D TS-TZFBR configurations is done, illustrating the role of the equivalent d_b definition on the bubble size profiles and further bubble characteristics. Pseudo-2D and 3D bubble measurements were carried out for a simulated Two-Section Two-Zone Fluidized Bed Reactor (Figure 1.b) at a relative gas velocity, $u_r = u_{gas}/u_{mf} = 2.5$ using Geldart-B particles ($d_p = 200$ μm, $\rho_p = 2.5$ g/cm^3) with $u_{mf} = 10.1$ cm/s.

4.1 Geometric 3D reconstruction of bubble topology

As it has been previously discussed, the accuracy of the geometric reconstruction of topological spaces based on α-shapes depends on the proper selection of a threshold α value to discriminate node connections in the 3D Delaunay triangulation mesh created from bubble contour nodes of CFD transient results. If a geometric reconstruction is not applied the triangulation method would connect every node under the Delaunay condition, leading to a unique mesh that does not discriminate individual bubbles. If α-shapes are applied, in principle the lower and more restrictive α value, the greater is the level of detail on individual bubble contours. Nevertheless, if the α threshold becomes lower than the edge length in the domain mesh, wrong topologies may be found. As an example, Figure 5 illustrates the effect of the α-shape value on the bubble contour detection for a transient simulated fluidization frame. Figure 5.a shows the iso-surface analysis performed to get the spatial coordinates of the bubble contour nodes. As already discussed, the iso-surface connects bed regions in which the solids volume fraction is 0.15 (or, analogously, the void fraction is 0.85). The planar iso-surface detected at the bed top represents the bed surface and, thus, it must be filtered out from the

hydrodynamic analysis (Figure 5.a). From left to right, Figure 5.b shows the number and shape of the detected gas bubbles by the 3D geometry reconstruction algorithm with increasing α-shape value. If the level of detail is greater than the mesh size, i.e. α < 0.25 cm, true node connections break leading to wrong bubble contour detection. In contrast, if α becomes higher than the mesh size the resolution of the method decreases resulting in bubble contour detection misleading.

The use of a fixed mesh along the time in the continuum Two-Fluid model simulations makes the selection of an appropriate α-shape value quite straightforward. This is not the case in meshless simulations of free surface flows, e.g. wave breaking [47], in which the selection of suitable α-shapes becomes troublesome.

4.2 Definition of 'equivalent bubble diameter'. Comparison between simulated bubble size profiles in pseudo-2D and 3D fluidized beds

Figures 6.a and 6.b show the evolution of the bubble size along the vertical bed position for the simulated 3D and pseudo-2D TS-TZFBR beds. Equations 6 and 8 have been used to calculate the equivalent diameter of raw bubbles from 3D reconstructed geometries and 2D projected areas, respectively. As can be observed in Figure 6.c, the time-averaged equivalent bubble diameter values are substantially greater in case of the pseudo-2D beds. This finding motivated the revision of the definition of 'equivalent bubble diameter'.

From the point of view of a pseudo-2D bed that aims to mimic a vertical slice of a cylindrical 3D bed through its bed center, the area-based bubble size of the 2D configuration should be compared with the planar projection of the 3D bed using Equation 8 to determine the equivalent bubble diameter.

From the point of view of the void volume enclosed by bubbles, the 3D bubble diameter measured by geometry reconstruction via α-shapes should be compared with the equivalent diameter of a sphere that occupies the same volume as that enclosed in the pseudo-2D bubble according to the definition given in Equation 9.

Figures 7.a and 7.b illustrate the comparison between time-averaged bubble size profiles obtained for 3D and pseudo-2D beds under the above considerations. For each case, the presented time-averaged d_b values have been calculated with respect to both the raw and the filtered bubble data.

Apparently, the effect of the spurious bubbles filtration on the computation of the time-averaged $d_b(z)$ profiles is negligible against the effect of the way to calculate d_b from simulation results. In general, the area-based definition of the bubble size leads to greater d_b values along the bed vertical position than the volume-based approach.

Image analysis from porosity maps (Figure 7.a) gives mimic $d_b(z)$ profiles for 2D and 3D configurations within the lower straight bed section. However, 2D simulations predict a substantial bubble size decrease along the tapered bed region and a fast bubble size growth within the upper straight bed zone, which are not observed in the porosity maps of the 3D configuration.

Regarding the volumetric formulation of the equivalent bubble diameter (Figure 7.b), the volume of bubbles from reconstructed 3D geometries is greater than that of pseudo-2D bubbles, with an average 23.2% overestimation on the equivalent bubble diameter. This agrees with the fact that for a same gas excess velocity in both configurations, $u_{gas} - u_{mf}$, the bubbles in the 3D bed (which has a greater cross-sectional area than the pseudo-2D reactor) carry a greater amount of gas. Nevertheless, the shape of the volume-based $d_b(z)$ profiles for 2D and 3D configurations is very similar and the bubble growing and shrinking trends along the 3D TS-TZFBR are qualitatively well reproduced by the pseudo-2D bed.

Summarizing the previous results it has been found that 2D simulations (and experiments in pseudo-2D beds, by extension) give valuable insight into the 3D bubbling regime although they are not able to mimic the characteristics of real 3D bubbles. Neither image analysis (area-based) techniques nor the pseudo-2D volume-based definition of the equivalent d_b can exactly reproduce the 3D bubble characteristics obtained by geometric reconstruction of 3D Two-Fluid Model simulations. Nevertheless, this second approach provides a much better agreement between $d_b(z)$ profiles at both reactor configurations. As a result, the proposed reconstruction of 3D bubbles using α-shapes leads to a more reliable and accurate description of the bubbling behaviour than the use of image analysis, i.e. tomography techniques [15, 27] for TFM simulated 3D fluidized beds.

4.3 3D bubble characteristics in a Two-Section Two-Zone Fluidized Bed Reactor

For each transient result of both pseudo-2D and 3D bed simulations, five different bubble parameters have been collected: equivalent diameter (according to equations 6 to 9), centroid coordinates, aspect ratio, bubbles hold-up and bed height. Additionally, bubble velocity values have been determined comparing bubble data between consecutive frames by a nearest-neighbour algorithm. The collected data along the simulation time have been used to perform a statistical analysis on the bubbling behaviour in a TS-TZFBR.

4.3.1 Radial distribution of bubble location along the 3D bed

The determination of bubble centroid coordinates allowed the study of the spatial distribution of bubbles within the TS-TZFBR. Figure 8.a shows a 3D scattered plot of the bubble centroid spatial location for eight seconds of simulated fluidization (sampling time, $\Delta t = 0.01s$). Results suggest that at the very bottom of the bed a great number of bubbles were formed close to the gas distributor. The bubbles that were initially distributed along the whole bed cross section flow towards the bed center upwards, where the lower presence of centroid points illustrates the bubble coalescence phenomenon. At the bottom-end of the tapered bed region ($z = z_{dis} = z_{sc} = 12$ cm), a high concentration of bubble centroids was found which is related to the incipient bubbles coming from the immersed gas distributor. As the bed cross-section area increases the number of bubbles decreased towards the freeboard, mainly due to coalescence and to the reduction of the gas excess over the minimum fluidization. The radial distribution map of bubble centroid location shown in Figure 8.b suggests that bubbles mainly flow up through the bed center and marginally close to the bed walls.

4.3.2 Bed expansion and void fraction in pseudo-2D and 3D TS-TZFBR configurations

Figure 9 shows the evolution of the bed height as well as the volume occupied by gas bubbles along the time on stream for the pseudo-2D and 3D bed configurations used in this work. Figure 9.c illustrates the axial fluctuation with time of the free bed surface due to the bubbling regime. The transient simulated bed height has been here determined measuring the average vertical coordinate of the upper contour line in 2D bed images (Figure 9.a) and of the upper meshed iso-surface in the 3D bed (Figure 9.b).

The average bed height gives an idea on the bed expansion whereas the amplitude and frequency of the fluctuation are related to bubble size and bubbling frequency, respectively.

Simulation results suggest that the average bed height of the pseudo-2D bed is 7.2% greater than that of the 3D bed ($z_{fb(2D)}$ = 31.3 cm and $z_{fb(3D)}$ = 29.2 cm) under the same fluidization conditions, as already observed by some authors [50]. Due to the special TS-TZFBR geometry, the bed expansion cannot be directly determined from the average fluidized bed height data. A volumetric formulation of the bed expansion needs to be used instead. Since the initial fixed bed height is the same (z_0 = 24 cm) for both configurations, the average volumetric bed expansion becomes $B_{e(3D)}$ = 1.50 and $B_{e(2D)}$ = 1.48 for the 3D and pseudo-2D bed, respectively. The deviation of the bed expansion between configurations results, thus, in a negligible 1.5%.

The transient evolution of the total gas volume enclosed by bubbles for both pseudo-2D and 3D beds is shown in Figure 9.c. The time-average bubbles hold-up (b_h) differs in less than 7% between reactor configurations, being $b_{h(2D)}$ = 13.2 cm^3 and $b_{h(3D)}$ = 12.3 cm^3. Since the cross-sectional area of the pseudo-2D is lower than that of the 3D reactor, a similar bed volume increase by means of gas bubbles resulted in an increased bed height in the case of the narrower reactor, as already observed. Therefore, there is no evidence to attribute the different fluidized bed height to solids packing being different in both reactor configurations.

4.3.3 Size probability distribution and bubbles aspect ratio

Although the transient evolution of the bubbles hold-up becomes very similar between both bed arrangements at the same fluidization conditions, the bubble size and shape distributions may not follow the same trend necessarily.

To illustrate that, the Figure 10.a shows that the pseudo-2D bed leads to a broader size distribution than the 3D configuration. The increased probability to find either very small (d_b < 0.4 cm) or big bubbles (d_b > 4 cm) in the pseudo-2D bed is in agreement with the results presented in Figures 6 and 7: the pseudo-2D bed shows a sharper $d_b(z)$ profile as a result of very small bubbles close to the immersed gas distributor and quite big bubbles close to the freeboard with respect to the 3D bed.

The bubble shape distribution or 'bubble aspect ratio' (*AR*), which is defined here as the ratio between bubble height and width, is strongly related to bubble velocity. On this regard, we expect that faster bubbles tend to be sharp (i.e. high *AR*) whereas slower bubbles are more flattered (i.e. low *AR*) [19]. Assuming that bubbles are faster in a 3D configuration, according to the classical formulation of Davidson and Harrison [51] (DH) depicted in equation 10, lower bubble aspect ratios are expected for the pseudo-2D configuration. The results shown in Figure 10.b are in agreement with this assumption.

$$u_{br} = (u_{gas} - u_{mf}) + u_b = (u_{gas} - u_{mf}) + K\sqrt{g\, d_b}\,, \qquad K = \begin{cases} 0.4\ (2D) \\ 0.71\ (3D) \end{cases} \tag{10}$$

4.3.4 Bubbles motion

In a conventional fluidized bed, the bubble velocity is proportional to the square root of the equivalent bubble diameter (equation 10) and bubbles grow axially in the bed. In previous works [34, 37], the authors have shown that this is not the case in a TS-TZFBR in which a tapered region and an immersed gas jet modify the $d_b(z)$ and, thus, the $u_b(z)$ and $u_b(d_b^{0.5})$ profiles. A new $d_{b,TS\text{-}TZFBR}(z)$ correlation was developed by Julián et al. [34] to account for the unconventional geometry of the reactor, i.e. the Julián-Herguido-Menéndez (JHM) model. This model, which couples the Mori and Wen $d_b(z)$ correlation [52] with the mass balance to the gas phase within the tapered bed region, is able to predict bubble size and velocity profiles in pseudo-2D TS-TZFBR.

Figure 11 shows a comparison between $u_b(z)$ and $u_b(d_b^{0.5})$ profiles at the two considered reactor configurations, as well as the prediction of the JHM+DH model for such velocity profiles. The TFM simulations were able to predict greater average bubble velocities in the 3D bed. Besides, the simulated average u_b values are in the range of these given by the semi-empirical correlations (JHM+DH) for both pseudo-2D and 3D bed.

It is important to remark that experimental measurements of 3D bubble properties are still not available in literature for TS-TZFBR configurations. Therefore, the computational formulation of the Two-Fluid Model used in this work cannot be validated against experimental data. However, to some extent the high agreement between the pseudo-2D and 3D $u_b(d_b)$ profiles in comparison to these predicted by the correlation of Davidson and Harrison (based on empirical values of the parameter K for their pseudo-2D and 3D measurements) suggests that the model is able to predict the experimental changes in the bubble properties as a function of the bed geometry.

5. Conclusions

In this work, an improved method to measure 3D bubbles from TFM simulations has been presented. The method deals with the volumetric discretization of connected bubble iso-contours by means of the so-called α-shapes. Compared to the tomographic techniques used in the open literature, this method provides a more reliable tool to analyze the bubble hydrodynamics in simulated 3D fluidized beds.

A critical comparison between the simulated bubble characteristics for a pseudo-2D and a 3D TS-TZFBR showed that the pseudo-2D bed gives a reasonably good estimation of the hydrodynamic behaviour in a 3D system. In particular the bed expansion, bubbles hold-up and bubble velocity profiles of the 3D TS-TZFBR could be directly estimated from pseudo-2D simulations.

Regarding the bubble size, the raw comparison between area-based $d_{b,pseudo\text{-}2D}(z)$ and volume-based $d_{b,3D}(z)$ profiles does not give a fair insight into the simulation model predictability and the validity of the α-shapes method. A volume-based formulation of the equivalent d_b for both

pseudo-2D and 3D beds is preferred. This formulation accounts for the effective volume of gas enclosed by bubbles. Using the volume-based d_b definition the average $d_b(z)$ profiles compared qualitatively well between reactor configurations. Nevertheless, the average $d_{b,pseudo\text{-}2D}$ overestimated $d_{b,3D}$ by 23.2% within the tapered bed region. This reveals that the bed geometry effectively plays role in the fluid dynamic behaviour of the TS-TZFBR.

6. Acknowledgement

Financial support from MINECO, Spain (Projects CTQ2010-15568 and ENE2013-44350-R) is gratefully acknowledged. Financial aid for the maintenance of the consolidated research group CREG has been provided by the Fondo Social Europeo (FSE) through the Gobierno de Aragón (Aragón, Spain).

Nomenclature

AR	Bubble aspect ratio, (-)
b_d	Bubble population density, ($n_{bub.}/cm^2s$)
B_e	Bed expansion, (-)
b_h	Bubbles holdup, (%)
C_D	Interphase drag coefficient, (-)
CFD	Computational Fluid Dynamics
d_b	Equivalent bubble diameter, (cm)
d_p	Particle diameter, (m)
DIA	Digital Image Analysis
e	Restitution coefficient, (-)
g	Acceleration due to gravity, (m/s^2)
g_0	Radial distribution function, (-)
$\bar{\bar{I}}$	Stress tensor, (-)
I_{2D}	Second invariant of the deviatory stress tensor, (-)
K	Bubble velocity coefficient, (-)
K_{gs}	Interphase momentum exchange coefficient, (kg/m^3s)
P	Pressure, (Pa)
PIV	Particle Image Velocimetry
Re	Reynolds number, (-)
TS-TZFBR	Two-Section Two Zone Fluidized Bed Reactor
TZFBR	Two-Zone Fluidized Bed Reactor
u_b	Single bubble velocity, (cm/s)
u_{br}	Bubbles velocity, (cm/s)
u_{gas}	Gas velocity, (cm/s)
u_{mf}	Minimum fluidization velocity, (cm^3/cm^2s)
$u_{r,bottom}$	Relative velocity (u_{gas}/u_{mf}) within the lower bed section, (-)
$u_{r,top}$	Relative velocity (u_{gas}/u_{mf}) within the upper bed section, (-)
$\vec{v}$	Local velocity, (m/s)
z_{dis}	immersed distributor axial location, (cm)
z_{sc}	TS-TZFBR section change axial location, (cm)

Greek symbols

α	Level of detail for the geometry in the alpha-shapes method, (-)
β	Defluidization angle, (^{o})
γ	Tapered section angle, (^{o})
γ_s	Collision dissipation energy, (kg/(m·s^3))
ε	Volume fraction, (-)
θ	Granular temperature, (m^2/s^2)
λ	Bulk viscosity, (kg/(m·s))
μ	Shear viscosity, (kg/(m·s))
μ_{col}	Collisional shear viscosity, (kg/(m·s))
μ_{kin}	Kinematic shear viscosity, (kg/(m·s))
μ_{fr}	Frictional shear viscosity, (kg/(m·s))
ρ	Density, [kg/m^3]
$\bar{\bar{\tau}}$	Stress-strain tensor, (kg/(m·s^2))
φ	Angle of internal friction in particle collisions, (^{o})
ω	Probability density of bubble size, (%)

Subscripts

i	Phase i, either fluid or solid
g	Fluid phase (gas)
s	Solid phase
m	maximum
0	initial

References

[1] Kunii, D.; Levenspiel, O. Fluidization engineering. Butterworth-Heinemann 1991.

[2] Busciglio, A.; Vella, G.; Micale, G.; Rizzuti, L. Analysis of the bubbling behaviour of 2D gas solid fluidized beds part I. digital image analysis technique. Chem. Eng. J. 140 (2008) 398-413.

[3] Laverman, J. A.; Roghair, I.; van Sint Annaland, M.; Kuipers, J. A. M. Investigation into the hydrodynamics of gas-solid fluidized beds using particle image velocimetry coupled with digital image analysis. Can. J. Chem. Eng. 86 (2008) 523-535.

[4] de Jong, J.F.; Odu, S. O.; van Buijtenen, M. S.; Deen, N. G.; van Sint Annaland, M.; Kuipers, J. A. M. Development and validation of a novel digital image analysis method for fluidized bed particle image velocimetry. Powder Technol. 230 (2012) 193-202.

[5] van Ommen, J.R.; Mudde, R.F. Measuring the gas-solids distribution in fluidized beds-A review. Int. J. Chem. React. Eng. 6 (2008) R3.

[6] Dyakowski, T.; Jaworski, A. J. Application of non-invasive techniques for imaging fluidized beds — A review. In: Handbook of Conveying and Handling of particulate solids Elsevier Science B.V. 10 (2001) 807-823.

[7] Mudde, R. F. Time-resolved X-ray tomography of a fluidized bed. Powder Technol. 199 (2010) 55-59.

[8] Laverman, J. A.; Fan, X.; Ingram, A.; van Sint Annaland, M.; Parker, D. J.; Seville, J. P. K.; Kuipers, J. A. M. Experimental study on the influence of bed material on the scaling of solids circulation patterns in 3D bubbling gas–solid fluidized beds of glass and polyethylene using positron emission particle tracking. Powder Technol. 224 (2012) 297-305.

[9] Fraguío, M. S.; Cassanello, M. C.; Larachi, F.; Limtrakul, S.; Dudukovic, M. Classifying flow regimes in three-phase fluidized beds from CARPT experiments. Chem. Eng. Sci. 62 (2007) 7523-7529.

[10] T. Hensler, M. Tupy, T. Strer, T. Pöschel, K.E. Wirth, Positron emission particle tracking in fluidized beds with secondary gas injection, Powder Technol. 279 (2015) 113-122.

[11] He, C.; Bi, X. T.; Grace, J. R. Simultaneous measurements of particle charge density and bubble properties in gas-solid fluidized beds by dual-tip electrostatic probes. Chem. Eng. Sci. 123 (2015) 11-21.

[12] Rüdisüli, M.; Schildhauer, T. J.; Biollaz, S. M. A.; van Ommen J. R. Bubble characterization in a fluidized bed by means of optical probes. Int. J. Multiphase Flow 41 (2012) 56-67.

[13] Bi, H. T. A critical review of the complex pressure fluctuation phenomenon in gas–solids fluidized beds. Chem. Eng. Sci. 62 (2007) 3473-3493.

[14] Rüdisüli, M.; Schildhauer, T. J.; Biollaz, S. M. A.; Van Ommen, J. R. 18 - measurement, monitoring and control of fluidized bed combustion and gasification. In: Fabrizio Scala, editor. Fluidized bed technologies for near-zero emission combustion and gasification. Woodhead Publishing; 2013. .

[15] Sobrino, C.; Acosta-Iborra, A.; Izquierdo-Barrientos, M. A.; de Vega, M. Three-dimensional two-fluid modeling of a cylindrical fluidized bed and validation of the maximum entropy method to determine bubble properties. Chem. Eng. J. 262 (2015) 628-639.

[16] van der Hoef, M. A.; Ye, M.; van Sint Annaland, M.; Andrews, A. T.; Sundaresan, S.; Kuipers, J. A. M. Multiscale modeling of gas-fluidized beds. Advances in Chem. Eng. 31 (2006) 65-149.

[17] Wang, L.; Zhang, B.; Wang, X.; Ge, W.; Li, J. Lattice boltzmann based discrete simulation for gas–solid fluidization. Chem. Eng. Sci. 101 (2013) 228-239.

[18] Deen, N. G.; Van Sint Annaland, M.; Van der Hoef, M. A.; Kuipers, J. A. M. Review of discrete particle modeling of fluidized beds. Chem. Eng. Sci. 62 (2007) 28-44.

[19] Busciglio, A.; Vella, G.; Micale, G.; Rizzuti, L. Analysis of the bubbling behaviour of 2D gas solid fluidized beds part II. comparison between experiments and numerical simulations via digital image analysis technique. Chem. Eng. J. 148 (2009) 145-163.

[20] Hernández-Jiménez, F.; Sánchez-Delgado, S.; Gómez-García, A.; Acosta-Iborra, A. Comparison between two-fluid model simulations and particle image analysis & velocimetry (PIV) results for a two-dimensional gas–solid fluidized bed. Chem. Eng. Sci. 66 (2011) 3753-3772.

[21] Asegehegn, T. W.; Schreiber, M.; Krautz, H. J. Numerical simulation and experimental validation of bubble behavior in 2D gas-solid fluidized beds with immersed horizontal tubes. Chem. Eng. Sci. 66 (2011) 5410-5427.

[22] Shen, L.; Johnsson, F.; Leckner, B. Digital image analysis of hydrodynamics two-dimensional bubbling fluidized beds. Chem. Eng. Sci. 59 (2004) 2607-2617.

[23] Hulme, I.; Clavelle, E.; van der Lee, L.; Kantzas, A. CFD modeling and validation of bubble properties for a bubbling fluidized bed. Ind. Eng. Chem. Res. 44 (2005) 4254-4266.

[24] Julián, I.; Herguido, J.; Menéndez, M. CFD model prediction of the two-section two-zone fluidized bed reactor (TS-TZFBR) hydrodynamics. Chem. Eng. J. 248 (2014) 352-362.

[25] Patil, D. J.; van Sint Annaland, M.; Kuipers, J. A. M. Critical comparison of hydrodynamic models for gas–solid fluidized beds—Part II: Freely bubbling gas–solid fluidized beds. Chem. Eng. Sci. 60 (2005) 73-84.

[26] A. Bakshi, C. Altantzis, R.B. Bates, A. F. Ghoniem, Eulerian-Eulerian simulation of dense solid-gas cylindrical fluidized beds: Impact of wall boundary condition and drag model on fluidization, Powder Technol. 277 (2015) 47-62

[27] Verma, V.; Deen, N. G.; Padding, J. T.; Kuipers, J. A. M. Two-fluid modeling of three-dimensional cylindrical gas–solid fluidized beds using the kinetic theory of granular flow. Chem. Eng. Sci. 102 (2013) 227-245.

[28] Verma, V.; Padding, J. T.; Deen, N. G.; Kuipers, J. A. M. Bubble formation at a central orifice in a gas–solid fluidized bed predicted by three-dimensional two-fluid model simulations. Chem. Eng. J. 245 (2014) 217-227.

[29] Edelsbrunner, H.; Mucke, E.P.. 3-dimensional alpha-shapes. Acm Transactions on Graphics 13 (1994) 43-72.

[30] Herguido, J.; Menéndez, M.; Santamaría, J. On the use of fluidized bed catalytic reactors where reduction and oxidation zones are present simultaneously. Catal. Today 100 (2005) 181-189.

[31] Pérez-Moreno, L.; Soler, J.; Herguido, J.; Menéndez, M. Stable Steam Reforming of Ethanol in a Two-Zone Fluidized-Bed Reactor. Ind. Eng. Chem. Res. 51 (2012) 8840-8848.

[32] Medrano, J. A.; Julián, I.; García, F.; Li, K.; Herguido, J.; Menéndez, M. Two-Zone Fluidized Bed Reactor (TZFBR) with palladium membrane for catalytic propane dehydrogenation: experimental performance assessment. Ind. Eng. Chem. Res. 52 (2013) 3723-3731.

[33] Gimeno, M. P.; Soler, J.; Herguido, J.; Menendez, M. Counteracting Catalyst Deactivation in Methane Aromatization with a Two Zone Fluidized Bed Reactor. Ind. Eng. Chem. Res. 49 (2010) 996-1000.

[34] Julián, I.; Herguido, J.; Menéndez, M. A non-parametric bubble size correlation for a two-section two-zone fluidized bed reactor (TS-TZFBR). Powder Technol. 256 (2014) 146-157.

[35] Julián, I.; Gallucci, F.; van Sint Annaland, M.; Herguido, J.; Menéndez, M. Hydrodynamic study of a two-section two-zone fluidized bed reactor with an immersed tube bank via PIV/DIA. Chem. Eng. Sci. 2015 (submitted).

[36] Julián, I.; Herguido, J.; Menéndez, M. Particle mixing in a two-section two-zone fluidized bed reactor. Experimental technique and counter-current back-mixing model validation. Ind. Eng. Chem. Res. 52 (2013) 13587-13596.

[37] Julián, I.; Gallucci, F.; van Sint Annaland, M.; Herguido, J.; Menéndez M. Coupled PIV/DIA for fluid dynamics studies on a two-section two-zone fluidized bed reactor. Chem. Eng. J. 207-208 (2012) 122-132.

[38] S. Cloete, S. T. Johansen, S. Amini, Investigation into the effect of simulating a 3D cylindrical fluidized bed on a 2D plane, Powder Technol. 239 (2013) 21-35.

[39] Cammarata, L.; Lettieri, P.; Micale, G. D. M.; Colman, D. 2D and 3D CFD simulations of bubbling fluidized beds using eulerian-eulerian models. Int. J. Chem. React. Eng. 1 (2003) A48.

[40] Gidaspow D. Multiphase flow and fluidization: Continuum and kinetic theory descriptions. Academic Press, San Diego 1994.

[41] L. Schiller, A. Naumann, A drag coefficient correlation, VDI Zeits 77 (1933) 318-320.

[42] C. K. K. Lun, S. B. Savage, D. J. Jeffrey, N. Chepurniy, Kinetic Theories for Granular Flow - Inelastic Particles in Couette-Flow and Slightly Inelastic Particles in a General Flowfield. J. Fluid Mech. 140 (1984) 223-256.

[43] C. K. K. Lun, S. B. Savage, The effects of an impact velocity dependent coefficient of restitution on stresses developed by sheared granular materials, Acta Mech. 63 (1986) 15–44.

[44] S. Cloete, A. Zaabout, S. T. Johansen, M. van Sint Annaland, F. Gallucci, S. Amini, The generality of the standard 2D TFM approach in predicting bubbling fluidized bed hydrodynamics, 235 (2013) 735-746.

[45] A. Bahramian, M. Olazar, G. Ahmadi, Effect of slip boundary conditions on the simulation of microparticle velocity fields in a conical fluidized bed, AIChE J., 59 (2013) 4502-4518.

[46] S. Cloete, S. Amini, S. T. Johansen, On the effect of cluster resolution in riser flows on momentum and reaction kinetic interaction, Powder Technol. 210 (2011) 6-17.

[47] Galavis, A.; González, D.; Alfaro, I.; Cueto, E. Improved boundary tracking in meshless simulations of free-surface flows. Comput. Mech. 42 (2008) 467-479.

[48] Patrick, E. A.; Fischer, F.P. A generalized k-nearest neighbor rule. Information and Control 16 (1970) 128-152.

[49] Asegehegn, T. W.; Schreiber, M.; Krautz, H. J. Investigation of bubble behavior in fluidized beds with and without immersed horizontal tubes using a digital image analysis technique. Powder Technol. 210 (2011) 5410-5427.

[50] Xie, N.; Battaglia, F.; Pannala, S. Effects of using two- versus three-dimensional computational modeling of fluidized beds: Part I, hydrodynamics. Powder Technol. 182 (2008) 1-13.

[51] Davidson, J.F.; Harrison, D. The behaviour of a continuously bubbling fluidised bed. Chem. Eng. Sci. 21 (1966) 731-738.

[52] Mori, S.; Wen, C.Y. Estimation of bubble diameter in gaseous fluidized-beds. AIChE J. 21 (1975) 109-115.

Table 1. Set of closure equations for the TFM simulation of a fluidized bed

Interphase momentum exchange coefficient:	$\begin{cases} K_{gs} = 150\frac{\varepsilon_s(1-\varepsilon_g)\mu_g}{\varepsilon_g {d_p}^2} + 1.75\frac{\varepsilon_s \rho_g \lvert\vec{v}_s-\vec{v}_g\rvert}{d_p} & (\varepsilon_g \leq 0.8) \\ K_{gs} = \frac{3}{4}C_D\frac{\varepsilon_s \rho_g \lvert\vec{v}_s-\vec{v}_g\rvert}{d_p}{\varepsilon_g}^{-1.65} & (\varepsilon_g > 0.8) \end{cases}$
→ *Drag coefficient:*	$\begin{cases} C_D = \frac{24}{\varepsilon_g Re_s}\left[1+0.15(\varepsilon_g Re_s)^{0.687}\right] & (Re_s \leq 1000) \\ C_D = 0.44 & (Re_s > 1000) \end{cases}$
→ *Reynolds number (solids):*	$Re_s = \frac{d_p \rho_g \lvert\vec{v}_s-\vec{v}_g\rvert}{\mu_g}$
Solids stress-strain tensor:	$\bar{\bar{\tau}}_s = \varepsilon_s\mu_s\left(\nabla\overrightarrow{v_s} + \nabla\overrightarrow{v_s}^T\right) + \varepsilon_s(\lambda_s - \frac{2}{3}\mu_s)\nabla\cdot\bar{v}_s\bar{\bar{I}}$
→ *Solids bulk viscosity*:	$\lambda_s = \frac{4}{3}{\varepsilon_s}^2\rho_s d_p g_0(1+e)\left(\frac{\theta}{\pi}\right)^{1/2}$
→ *Solids shear viscosity*:	$\mu_s = \mu_{s,col} + \mu_{s,fr} + \mu_{s,kin}$
→ *Collisional viscosity*:	$\mu_{s,col} = \frac{4}{5}{\varepsilon_s}^2\rho_s d_p g_0(1+e)\left(\frac{\theta}{\pi}\right)^{1/2}$
→ *Kinetic viscosity*:	$\mu_{s,kin} = \frac{5\rho_s d_p\sqrt{\theta\pi}}{48 g_0(1+e)}\left[1+\frac{4}{5}g_0\varepsilon_s(1+e)\right]^2$
→ *Frictional viscosity*:	$\mu_{s,fr} = \frac{P_s \sin\varphi}{2\sqrt{I_{2D}}}$
→ *Radial distribution function*:	$g_0 = \left[1-(\frac{\varepsilon_s}{\varepsilon_{s,m}})^{1/3}\right]^{-1}$
→ *Algebraic equilibrium model (θ)*:	$\bar{\bar{\tau}}_s\,\nabla\overrightarrow{v_s} = \gamma_s$ *(Production = Dissipation)*
→ *Collisional dissipation of energy*:	$\gamma_s = \frac{12(1-e^2)g_0}{d_p\sqrt{\pi}}\rho_s{\varepsilon_s}^2\theta^{3/2}$
Solids pressure:	$P_s = \varepsilon_s\rho_s\theta\left(1+2\,\varepsilon_s g_0(1+e)\right)$

Table 2. List of model parameters used in the *CFD* simulation

Model parameter	Value
Reactor height (cm)	50
Particle density, ρ_s (kg/m^3)	2500
Particle diameter, d_p (μm)	200
Mesh-to-particle size, (-)	≤ 12
Initial solids volume fraction, ε_{s0} (-)	0.25
Maximum packing fraction, $\varepsilon_{s,m}$ (-)	0.65
Restitution coefficient, e (-)	0.95
Gas temperature (^{o}C)	25

FIGURE CAPTIONS

Figure 1. a) Scheme of a 3D TS-TZFBR, b) Simulated TS-TZFBR dimensions (in centimeters), c) Domain mesh

Figure 2. a) 2D porosity distribution map, b) 3D bubble detection as threshold porosity iso-surface, c) Detail of detected 3D bubbles, d) Meshed bubble contours, e) Delaunay triangulation (tetrahedral)

Figure 3. Tetrahedron coordinates

Figure 4. Area-based equivalent bubble diameter for: a) 3D TS-TZFBR, b) pseudo-2D TS-TZFBR. c) Volume-based d_b for a pseudo-2D TS-TZFBR

Figure 5. a) Detected bubble contours as iso-surfaces with a solids volume fraction, ε_s = 0.15. b) Effect of the α-value on the bubbles discretization

Figure 6. Axial evolution of the equivalent bubble diameter in a TS-TZFBR at u_{gas}/u_{mf} = 2.5. a) volume-based d_b for a 3D TS-TZFBR, b) area-based d_b for a pseudo-2D TS-TZFBR, c) time-averaged $d_b(z)$ profiles for 3D and pseudo-2D configurations. Dots and circles represent raw and time-averaged $d_b(z)$ values, respectively

Figure 7. Comparison between time-averaged $d_b(z)$ profiles for 3D and pseudo-2D configurations using: a) an area-based d_b, b) a volume-based d_b

Figure 8. a) Spatial distribution of bubble centroids in the bed, b) Radial probability distribution of the bubble centroid location (PD_r)

Figure 9. Free bed surface detection for: a) pseudo-2D bed, b) 3D bed. c) Transient evolution of the free bed surface axial location and gas content in bubbles (or void bed volume)

Figure 10. Probability distribution of: a) bubble size, b) bubble aspect ratio for the pseudo-2D and 3D TS-TZFBR

Figure 11. Bubble velocity profiles: a) $u_b(z)$, b) $u_b(d_b^{0.5})$ for the pseudo-2D and 3D TS-TZFBR

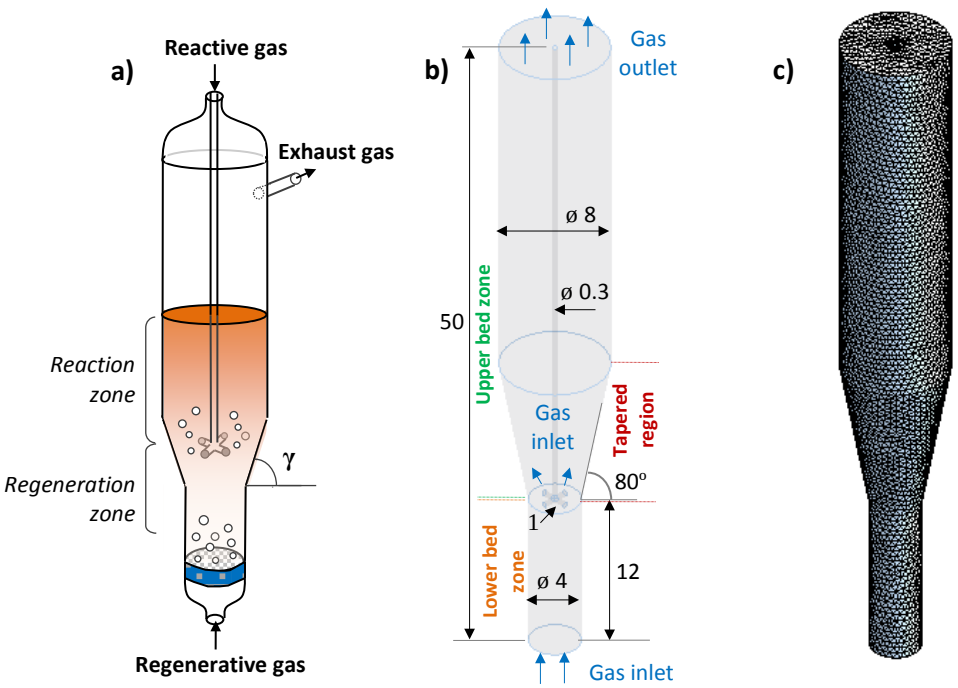
a)
Reactive gas
Exhaust gas
Reaction zone
Regeneration zone
γ
Regenerative gas
b)
Gas outlet
ø 8
ø 0.3
50
Upper bed zone
Gas inlet
Tapered region
80°
1
Lower bed zone
ø 4
12
Gas inlet
c)

Figure 1.

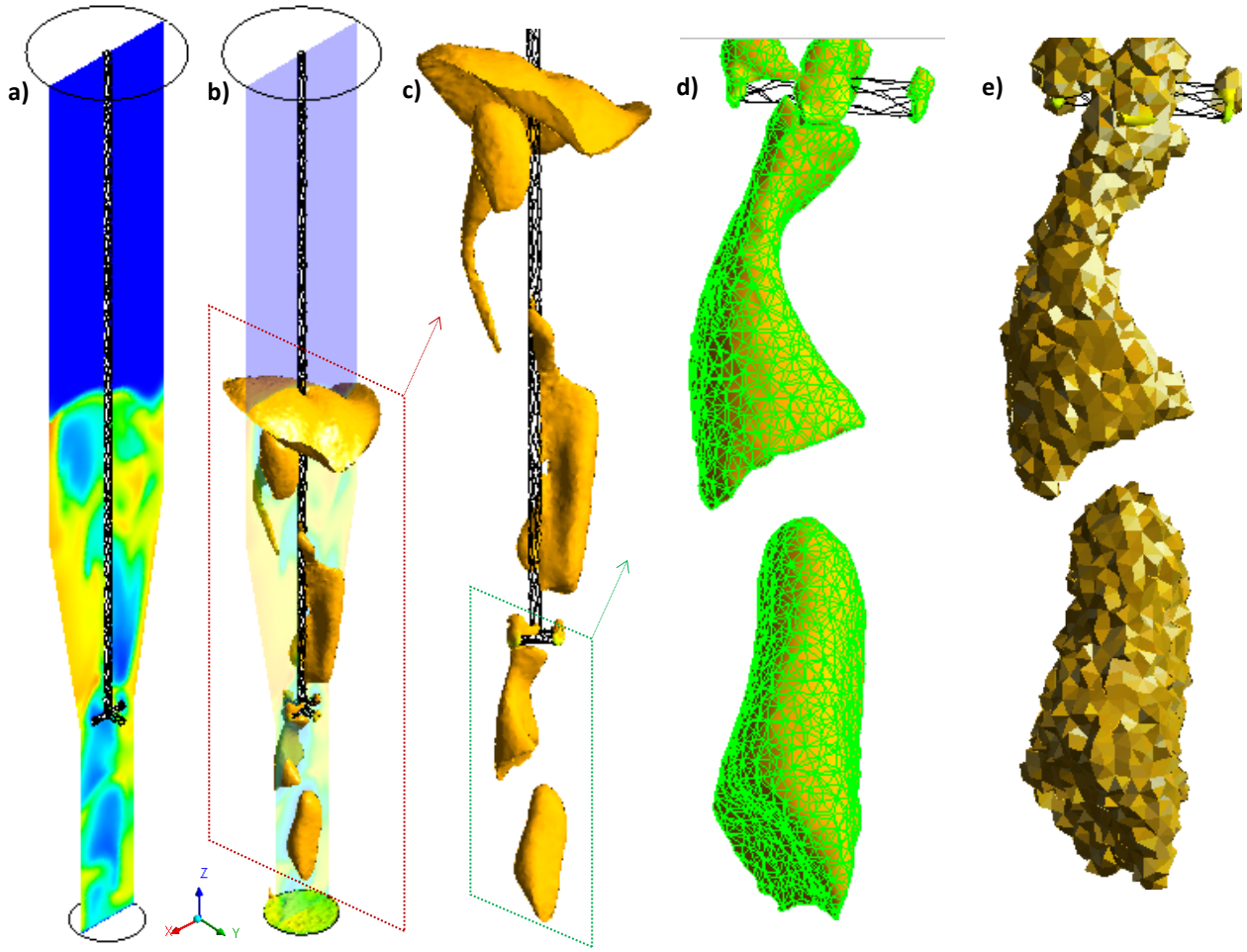

Figure 2.

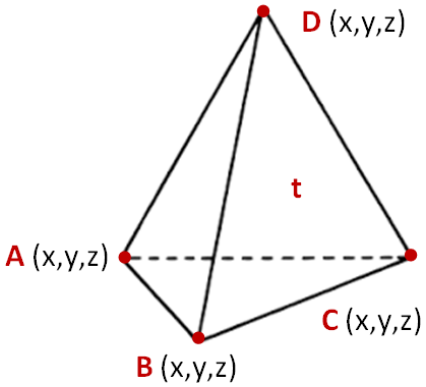

Figure 3.

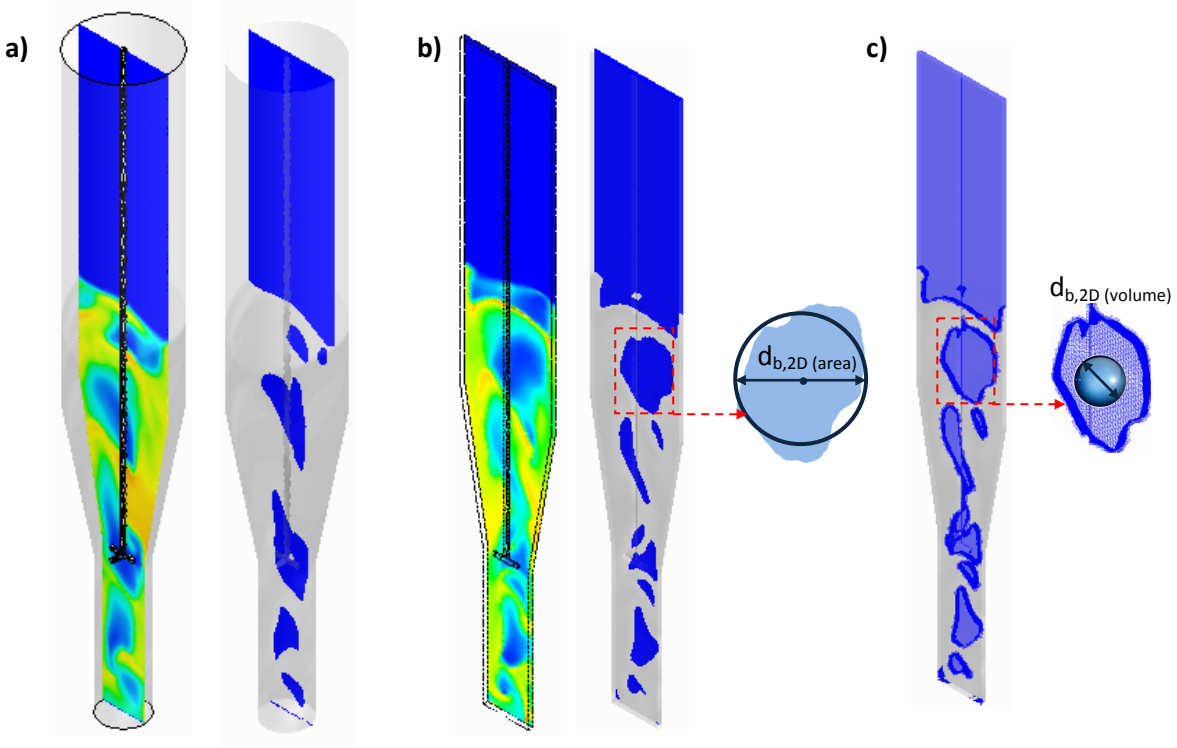

Figure 4.

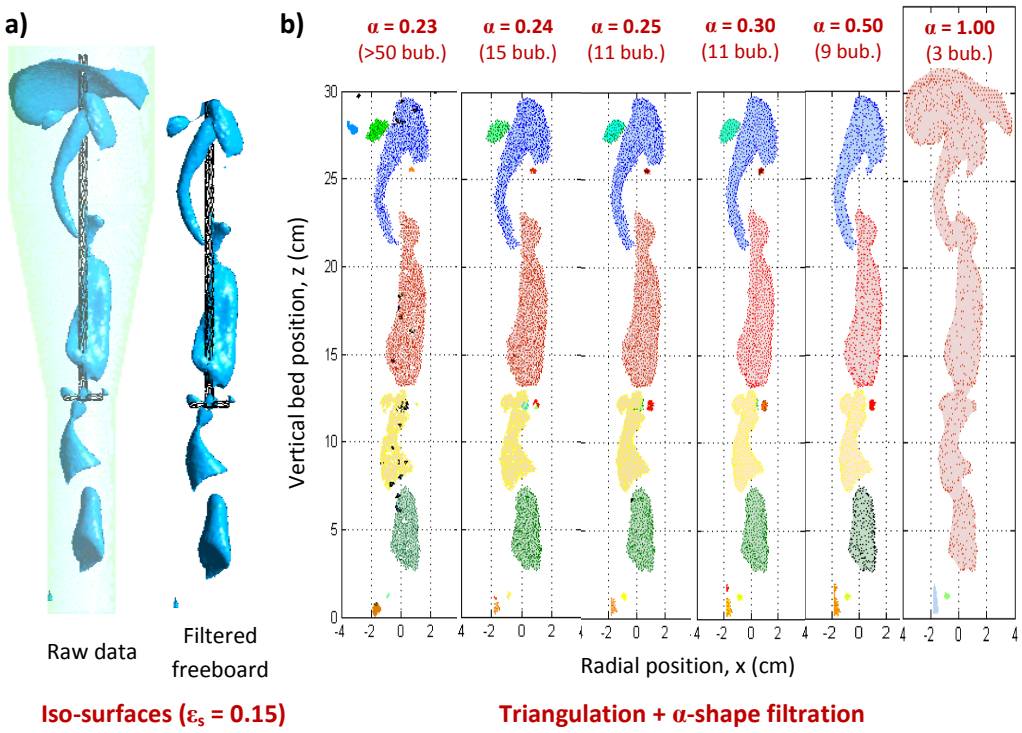
a)
b)
α = 0.23
(>50 bub.)
α = 0.24
(15 bub.)
α = 0.25
(11 bub.)
α = 0.30
(11 bub.)
α = 0.50
(9 bub.)
α = 1.00
(3 bub.)
Vertical bed position, z (cm)
Radial position, x (cm)
Raw data
Filtered freeboard
Iso-surfaces (εs = 0.15)
Triangulation + α-shape filtration

Figure 5.

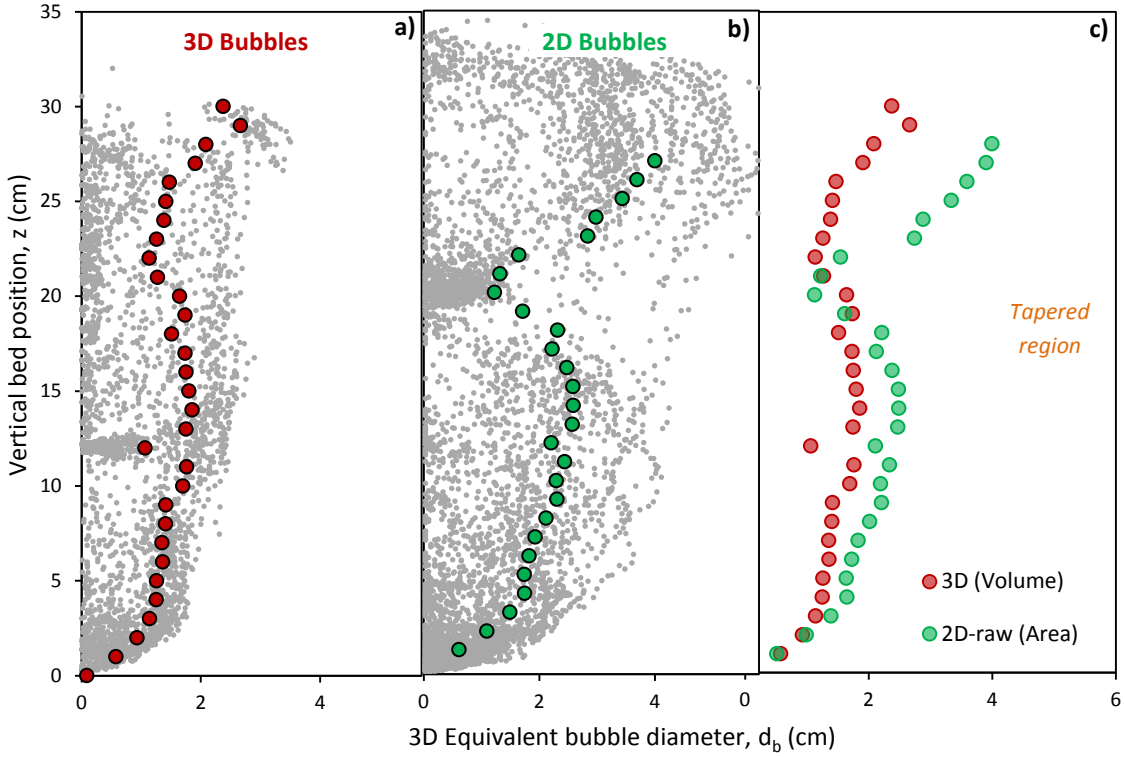
3D Bubbles
a)
2D Bubbles
b)
c)
Tapered region
3D (Volume)
2D-raw (Area)
Vertical bed position, z (cm)
3D Equivalent bubble diameter, d_b (cm)
0
5
10
15
20
25
30
35
0
2
4
6

Figure 6.

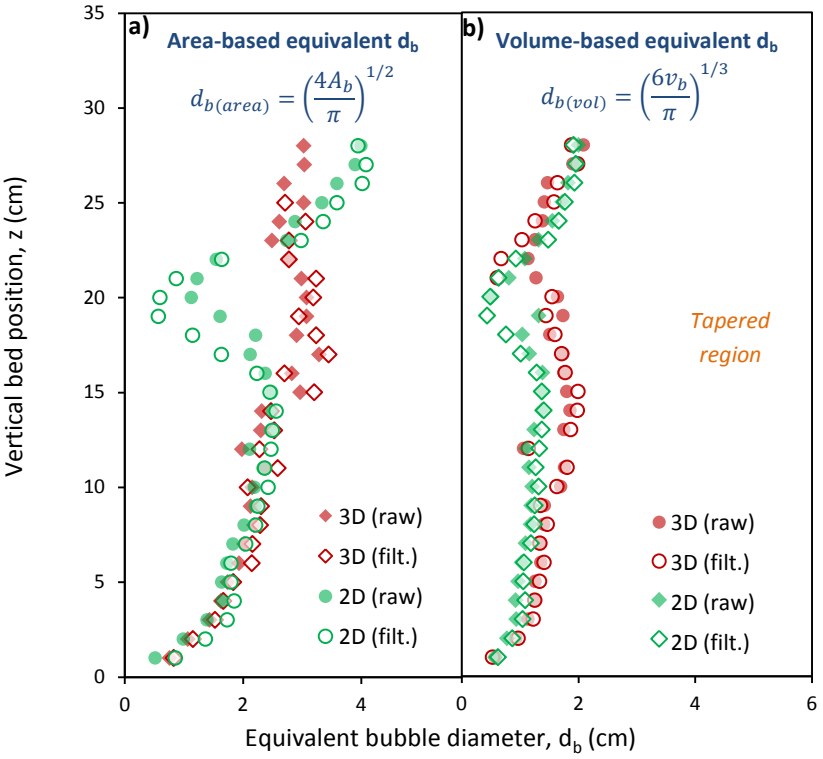
a)
Area-based equivalent d_b
$d_{b(area)} = \left(\frac{4A_b}{\pi}\right)^{1/2}$
b)
Volume-based equivalent d_b
$d_{b(vol)} = \left(\frac{6v_b}{\pi}\right)^{1/3}$
Tapered region
3D (raw)
3D (filt.)
2D (raw)
2D (filt.)
Vertical bed position, z (cm)
Equivalent bubble diameter, d_b (cm)
0
5
10
15
20
25
30
35
0
2
4
6

Figure 7.

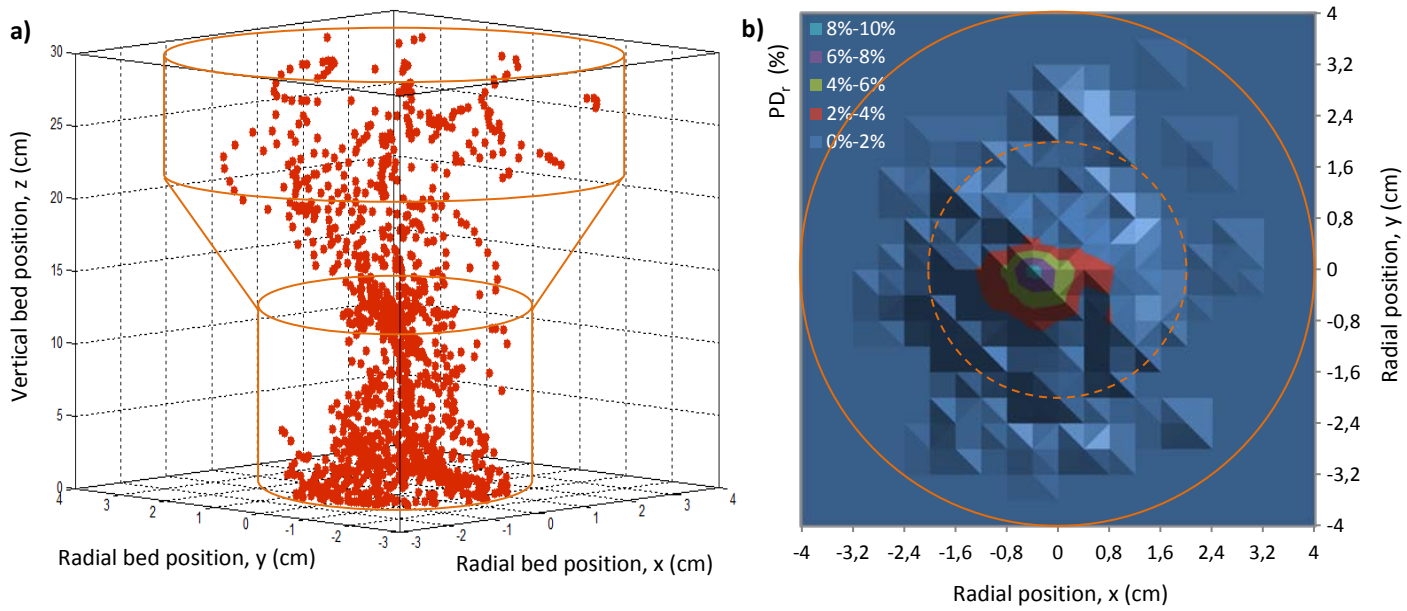
a)
Vertical bed position, z (cm)
Radial bed position, y (cm)
Radial bed position, x (cm)
b)
8%-10%
6%-8%
4%-6%
2%-4%
0%-2%
PDf (%)
Radial position, x (cm)
Radial position, y (cm)

Figure 8.

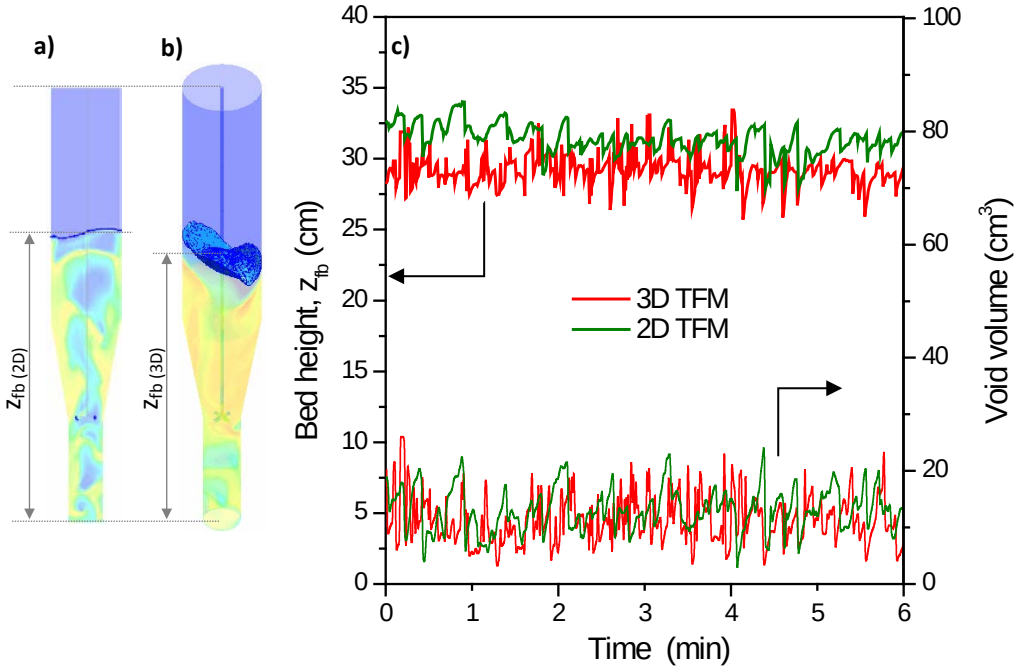
a)
b)
c)
$z_{fb\ (2D)}$
$z_{fb\ (3D)}$
Bed height, z_{fb} (cm)
Void volume (cm^3)
Time (min)
3D TFM
2D TFM
0
5
10
15
20
25
30
35
40
0
20
40
60
80
100
0
1
2
3
4
5
6

Figure 9.

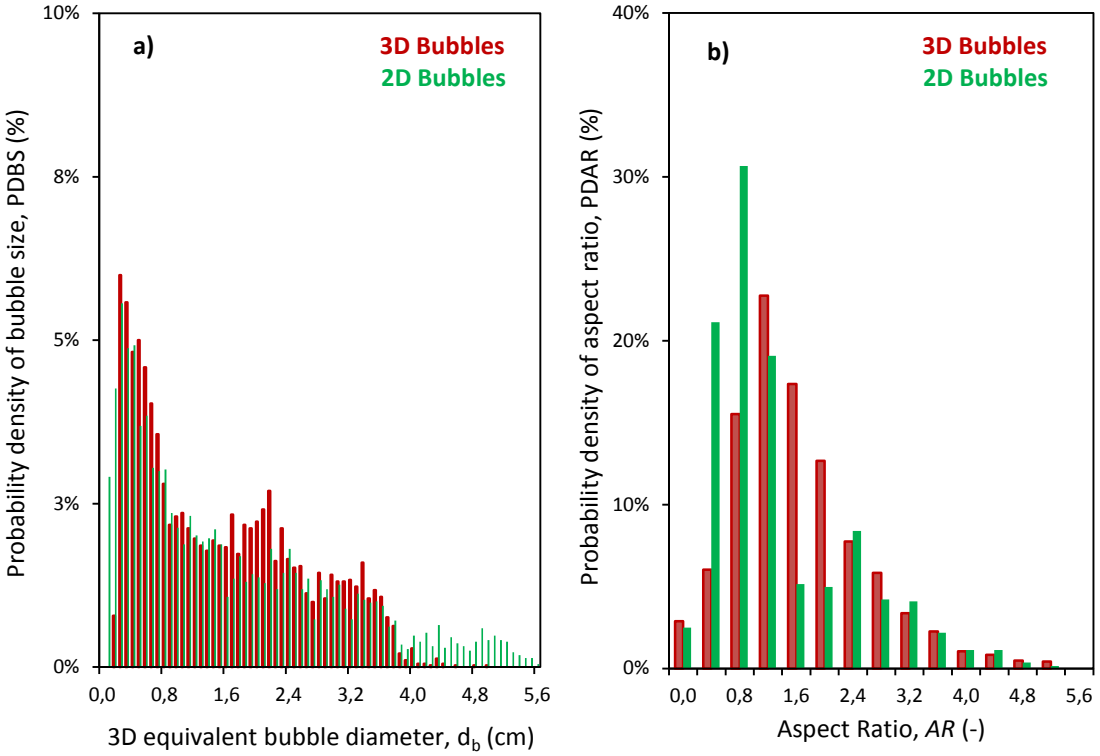
a)
3D Bubbles
2D Bubbles
Probability density of bubble size, PDBS (%)
10%
8%
5%
3%
0%
0,0
0,8
1,6
2,4
3,2
4,0
4,8
5,6
3D equivalent bubble diameter, d_b (cm)
b)
3D Bubbles
2D Bubbles
Probability density of aspect ratio, PDAR (%)
40%
30%
20%
10%
0%
0,0
0,8
1,6
2,4
3,2
4,0
4,8
5,6
Aspect Ratio, *AR* (-)

Figure 10.

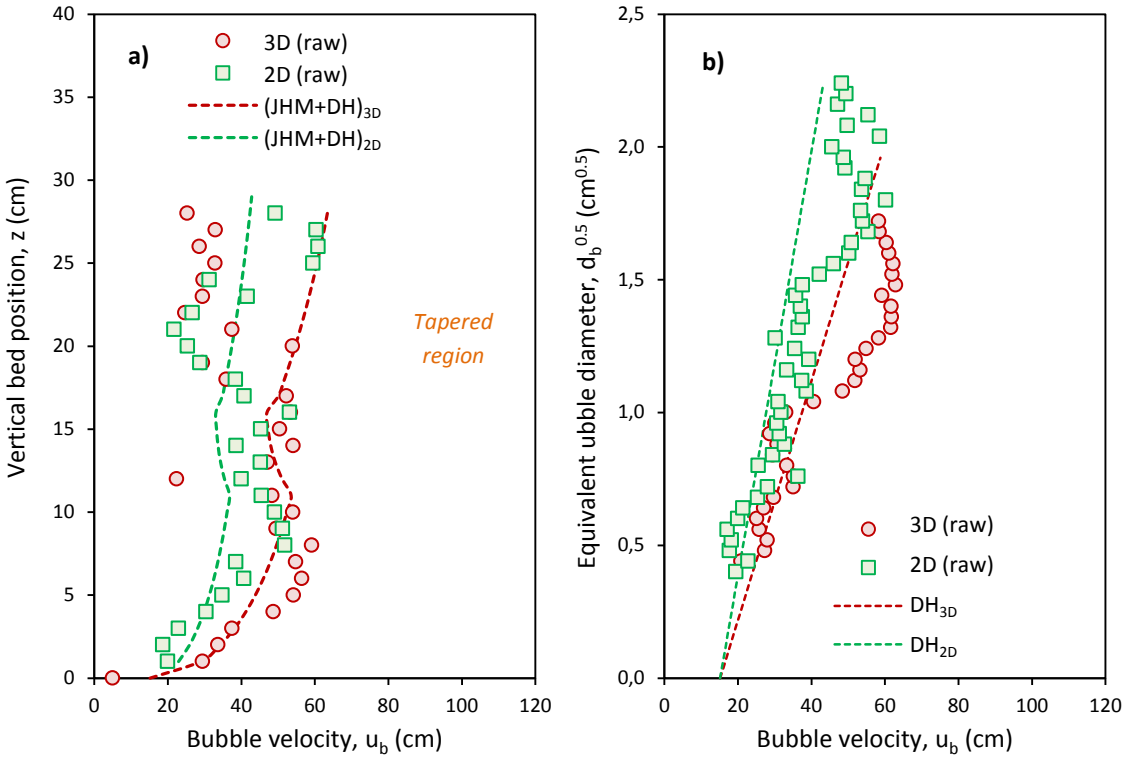
a)
3D (raw)
2D (raw)
(JHM+DH)3D
(JHM+DH)2D
Tapered region
Vertical bed position, z (cm)
Bubble velocity, ub (cm)
b)
3D (raw)
2D (raw)
DH3D
DH2D
Equivalent ubble diameter, db0.5 (cm0.5)
Bubble velocity, ub (cm)

Figure 11.